

Electron-boson glue function derived from electronic Raman scattering

B. Muschler,¹ W. Prestel,¹ E. Schachinger,^{2,*} J. P. Carbotte,^{3,4} R. Hackl,¹ Shimpei Ono,⁵ and Yoichi Ando⁶

¹Walther Meissner Institut, Bayerische Akademie der Wissenschaften, 85748 Garching, Germany

²Institute of Theoretical and Computational Physics,
Graz University of Technology, A-8010 Graz, Austria

³Department of Physics and Astronomy, McMaster University, Hamilton, Ontario N1G 2W1, Canada

⁴The Canadian Institute for Advanced Research, Toronto, Ontario M5G 1Z8, Canada

⁵Central Research Institute of Electric Power Industry, Yokosuka, Kanagawa 240-0196, Japan

⁶Institute of Scientific and Industrial Research, Osaka University, Ibaraki, Osaka 567-0047, Japan

Raman scattering cross sections depend on photon polarization. In the cuprates nodal and antinodal directions are weighted more strongly in B_{2g} and B_{1g} symmetry, respectively. On the other hand in angle-resolved photoemission spectroscopy (ARPES), electronic properties are measured along well-defined directions in momentum space rather than their weighted averages. In contrast, the optical conductivity involves a momentum average over the entire Brillouin zone. Newly measured Raman response data on high-quality $\text{Bi}_2\text{Sr}_2\text{CaCu}_2\text{O}_{8+\delta}$ single crystals up to high energies have been inverted using a modified maximum entropy inversion technique to extract from B_{1g} and B_{2g} Raman data corresponding electron-boson spectral densities (glue) are compared to the results obtained with known ARPES and optical inversions. We find that the B_{2g} spectrum agrees qualitatively with nodal direction ARPES while the B_{1g} looks more like the optical spectrum. A large peak around 30 – 40 meV in B_{1g} , much less prominent in B_{2g} , is taken as support for the importance of (π, π) scattering at this frequency.

PACS numbers: 74.20.Mn, 74.72.Gh, 78.30.-j

Boson structures seen in tunneling and to a lesser extent in optics in conventional superconductors have given us detailed information about the electron-phonon interaction in these materials. While similar structures have been identified in the cuprates in tunneling, point contact junctions¹ as well as scanning tunneling spectroscopy (STS)^{2,3}, in angle-resolved photo emission (ARPES)⁴⁻¹⁰, and, particularly, in optics¹¹⁻¹⁴, some of the details associated with the recovered electron-boson spectral density remain controversial, particularly the nature of the bosons involved. Some investigators stress the role of phonons¹⁻⁷ while others favour spin fluctuations⁸⁻¹⁴. Of course, both mechanisms are expected to contribute to the effective electron-boson interaction so that the debate really centers on which might be dominant¹⁴⁻¹⁶. Recent ARPES data have found a 6% softening of the boson ‘kink’ in the nodal direction renormalized electronic dispersion curves for $\text{Bi}_2\text{Sr}_2\text{CaCu}_2\text{O}_{8+\delta}$ ($\text{Bi}2212$) compounds on substitution of ^{16}O by ^{18}O ^{15,16}. Based on an examination of the detailed shape of the electron-boson spectral function, $I^2\chi(\omega)$, (glue function) obtained from a maximum entropy inversion¹⁷ of data on a similar sample¹⁰ of $\text{Bi}2212$, Schachinger *et al.*¹⁵ have argued that the isotope substitution data can be understood if a peak seen in the electron-boson spectral density $I^2\chi(\omega)$ around 65 meV which contains about 10% of the total area is assigned to an oxygen phonon mode. This leaves 90% of the effective spectrum which extends to 400 meV, much larger than any phonon energy, to possibly come from spin fluctuations.

So far $I^2\chi(\omega)$ has been recovered from tunneling^{1,18}, nodal direction ARPES^{6-8,10}, and optical data in the cuprates^{11-14,19,20}. In principle, $I^2\chi(\omega)$ is anisotropic

and it will be different for each momentum direction. Also quasiparticle and optical spectral densities will not be the same. While both involve the same bosons different weighting electronic factors apply. This is also true for Raman for which different vertices apply for different photon polarization²¹⁻²⁶. Nevertheless, it is important to obtain the corresponding electron-boson spectral density associated with B_{1g} and B_{2g} Raman data and to understand how these might differ from those obtained from ARPES and from optics and to establish points of consistency between these various spectra. Based on a memory function approach to the Raman cross section²⁵ one can extract a corresponding Raman scattering rate which depends on polarization. In this work we apply a maximum entropy inversion technique to extract from such data a spectral density in analogy to what is done for the infrared conductivity.

The analysis starts from new experimental results from freshly prepared high-quality single crystals of $\text{Bi}_2\text{Sr}_2\text{CaCu}_2\text{O}_{8+\delta}$. The crystals were grown in a mirror furnace using the traveling-solvent floating-zone (TSFZ) technique and post-annealed at 870 °C to arrive at optimal doping ($p = 0.16$ holes/ CuO_2) with a T_c of 94.5 K and a transition width below 1 K. The quality of the samples is crucial since defects lead to a strongly enhanced cross section at high energies²⁷.

The basis of the analysis is the Raman response function $R_\mu\chi''_\mu(T, \omega)$, where μ represents the scattering symmetry. Here we focus on $\mu = B_{1g}$ and B_{2g} . The response is derived from the measured cross section σ_μ as $R_\mu\chi''_\mu = (\omega_I/\omega_S)[1 + n(\omega, T)]^{-1}d^2\sigma_\mu/(d\Omega d\omega_S)$ ²⁶. Here, $\omega_{I,(S)}$ is the frequency of the incident (scattered) light. Ω is the solid angle of acceptance of the collection optics

and $n(\omega, T) = \{\exp[\hbar\omega/(k_B T) - 1]\}^{-1}$ is the Bose factor. σ_μ is corrected for the sensitivity of the instrument. Since the optical constants vary only little for visible light, interface effects can be absorbed in the constant R_μ the magnitude of which is irrelevant here. For revealing the pure symmetry components of the response in a reliable fashion we measured spectra at all six main polarizations of the ab -plane. This allows us to check the internal consistency of the procedure. Thus, the B_{1g} response, for example, reads in a short hand notation

$$B_{1g} = \frac{1}{3} \left[xx + x'y' + RL - \frac{1}{2}(RR + xy + x'x') \right], \quad (1)$$

where $x = [100]$, $x' = [110]$, $R = [100] + i[010]$, etc. The typical number of photon counts per point is between 1000 and 10000 which results in a relative statistical error in the range of one to three percent. For the experiments shown here the read-out noise of the CCD detector is negligible.

Opel *et al.*²⁵ show how a Raman scattering rate, $\Gamma_\mu(T, \omega)$, can be extracted quantitatively from $R_\mu \chi''_\mu(T, \omega)$. At a given symmetry the sensitivity in momentum space is uniquely defined, and the main contributions in B_{1g} and B_{2g} symmetry come from the region close to $(\pi, 0)$ (and equivalent points of the Brillouin zone) and from the center of the quadrant, respectively. The derived scattering rates $\Gamma_\mu(T, \omega)$ are analogous to the optical scattering rate, $\tau_{\text{opt}}^{-1}(T, \omega)$, obtained from infrared measurements¹¹ but correspond to different parts of the BZ dictated by symmetry μ ²⁶. In the normal state and within a Kubo formalism we can show that the Raman spectrum²⁴ and the optical response²⁸⁻³² is related to the appropriate electron-boson spectral density, $I_\mu^2 \chi(\nu)$, to a good approximation through the equation³³⁻³⁵

$$\Gamma_\mu(T, \omega) - \tau_{\mu, \text{imp}}^{-1} = \int_0^\infty d\nu K(\omega, \nu; T) I_\mu^2 \chi(\nu), \quad (2)$$

where $\tau_{\mu, \text{imp}}^{-1}$ is a Raman impurity scattering rate and

$$K(\omega, \nu; T) = \frac{\pi}{\omega} \left[2\omega \coth\left(\frac{\nu}{2T}\right) - (\omega + \nu) \coth\left(\frac{\omega + \nu}{2T}\right) + (\omega - \nu) \coth\left(\frac{\omega - \nu}{2T}\right) \right], \quad (3)$$

where T denotes the temperature. For the conductivity which involves an average over all momentum directions θ the appropriate electron-boson spectral density is $I_\mu^2 \chi(\nu) = \langle I_\mu^2 \chi(\nu, \theta) \rangle_\theta$ with $\langle \dots \rangle_\theta$ the average over the directions θ . For the Raman case with symmetry μ there is an additional weighting of $\cos^2(2\theta)$ for B_{1g} and $\sin^2(2\theta)$ for B_{2g} . Here, $I_\mu^2 \chi(\nu, \theta)$ is the electron-boson spectral density associated with momentum direction θ . There is another difference between quasiparticle and transport quantities associated with vertex corrections.

These are expected to mainly change the magnitude of the distribution functions with shape changes secondary.

Jiang and Carbotte²⁴ give the formula for the lowest order Raman susceptibility for an interacting electron system in the form

$$\chi_\mu(i\nu_n) = -T \sum_m \sum_{\mathbf{q}} \text{Tr} [\gamma_\mu^2(\mathbf{q}) \tau_3 \mathcal{G}(\mathbf{q}, i\omega_m) \tau_3 \mathcal{G}(\mathbf{q}, i\omega_m - i\nu_n)], \quad (4)$$

with ω_m and ν_n the fermionic and bosonic Matsubara frequencies, respectively, \mathbf{q} the momentum vector, τ_3 the third Pauli matrix and $\mathcal{G}(\mathbf{q}, i\omega_m)$ the electronic matrix Green's function in Nambu notation. Equation (4) is valid in the superconducting as well as normal state. Here we consider only the latter. Equation (4) differs from the well known formula for the optical conductivity^{24,28-31} only through the factor $\gamma_\mu^2(\mathbf{q})$, Ref.²⁴, which is to be replaced by $e^2 v_{F,x}^2(\mathbf{q})$ where $v_{F,x}(\mathbf{q})$ is the x -component of the Fermi velocity at momentum \mathbf{q} which in the free electron model is assumed constant and $v_{F,x}^2(\mathbf{q}) = v_F^2/2$ in two dimensions. For infinite bands with constant electronic density of states $N(0)$, Eq. (4) can be written in a more convenient form as

$$\chi_\mu(i\nu_n \rightarrow \nu + i0^+) = N(0) \int_{-\infty}^{\infty} d\epsilon \int_0^{2\pi} \frac{d\theta}{2\pi} \times \frac{[f(\epsilon) - f(\epsilon - \nu)] \gamma_\mu^2(\theta)}{\nu + i\tau_{\mu, \text{imp}}^{-1} + \Sigma^*(\epsilon, \theta) - \Sigma(\epsilon + \nu, \theta)}. \quad (5)$$

This equation has the same form as Eq. (22) of Sharapov and Carbotte³⁵ reported in their study of the effect of the energy dependence of the quasiparticle density of states on the far-infrared absorption in underdoped cuprates. Equation (5) differs as there is now an integration over angles θ , the additional Raman vertex $\gamma_\mu^2(\theta)$, and a different numerical factor. The same algebraic manipulation as is applied in Ref.³³ gives:

$$\Gamma_\mu(\omega) = \tau_{\mu, \text{imp}}^{-1} - \frac{1}{\omega} \int_{-\infty}^{\infty} d\epsilon [f(\epsilon) - f(\epsilon + \omega)] \times \int_0^{2\pi} \frac{d\theta}{2\pi} \gamma_\mu^2(\theta) \text{Im} [\Sigma_\mu(\epsilon + \omega, \theta) - \Sigma_\mu^*(\epsilon, \theta)], \quad (6)$$

where $\Sigma_\mu(\epsilon, \theta)$ is the quasiparticle self energy due to the directional electron-boson spectral density $I_\mu^2 \chi(\Omega, \theta)$ and the \star indicates the complex conjugate. This leads directly to our fundamental Eq. (2) when we use the relationship for the imaginary part of the quasiparticle self energy in

terms of $I^2\chi(\Omega, \theta)$, namely

$$\text{Im}\Sigma_\mu(\omega, \theta) = -\frac{\pi}{2} \int_0^\infty d\Omega I_\mu^2\chi(\Omega, \theta) \left[2\coth\left(\frac{\Omega}{2T}\right) - \tanh\left(\frac{\omega + \Omega}{2T}\right) + \tanh\left(\frac{\omega - \Omega}{2T}\right) \right]. \quad (7)$$

In the approximation of Eq. (5) for $\chi_\mu(\omega)$ we can construct the corresponding Raman cross section from

$$\text{Im}\chi_\mu(\omega) = \chi_\mu''(\omega) = \frac{\omega\Gamma_\mu(\omega)}{\{\omega[1 + \lambda_\mu(\omega)]\}^2 + \Gamma_\mu^2(\omega)}, \quad (8)$$

where $\omega\lambda_\mu(\omega)$ is the Kramers-Kronig transform (KK) of $\Gamma_\mu(\omega)$ as described by Opel *et al.*²⁵ [Eq. (A8)] to whom we refer for a detailed discussion of how the scattering rate $\Gamma_\mu(\omega)$ is extracted from the data on the Raman cross section corresponding to B_{1g} and B_{2g} symmetries. In Fig. 1 we present our results for the electron-boson spectral density $I_\mu^2\chi(\omega)$, Fig. 1(a) for B_{1g} (antinodal) and Fig. 1(b) B_{2g} (nodal) polarizations. We show for comparison equivalent results obtained previously from optics^{17,36}, Fig. 1(c), and from nodal direction ARPES, Ref.¹⁰, Fig. 1(d). In Fig. 2(a) we show our maximum entropy fits to the B_{2g} Raman scattering rates for two temperatures. The light solid (blue) dots are experiment at $T = 98$ K and the heavy solid (black) curve our fit. The light open (black) dots give the data for $T = 298$ K with the heavy dashed (red) curve our fit. Note that the low frequency part of the data at 98 K is almost linear, a feature which is well captured by the theoretical fit except for the very lowest ω region. On the whole the general trend is well described by our data reconstruction. To compensate for the rather big zero frequency offset of $\Gamma_{B_{2g}}(\omega \rightarrow 0, T)$ an impurity scattering rate of $\tau_{B_{2g},imp}^{-1} = 44$ meV had to be introduced in Eq. (2). In Fig. 2(b) we show a comparison between data and theoretical fit for the B_{2g} Raman cross section (see Ref.²⁵ for notation) which is the measured quantity from which the Raman scattering rate $\Gamma_{B_{2g}}(T, \omega)$ of Fig. 2(a) has been extracted. To get this quantity we applied Eq. (8), with $\lambda_{B_{2g}}(T, \omega)$ obtained from a Kramers-Kronig transform of our fitted Raman scattering rate $\Gamma_{B_{2g}}(T, \omega)$. We see good agreement except for a low frequency peak in the theoretical curve at $T = 98$ K [heavy solid (black) curve] not present in the data. This peak is traced to our use of an infinite band approximation. The experimental data on $\Gamma_\mu(T, \omega)$ develop peaks around 700 meV (not shown here) for both B_{1g} and B_{2g} symmetry which is understood to be the result of a reduction in the electronic density of states as a band edge¹⁰ is approached. This effect is not captured in our calculations and translates into important differences between calculated and experimental $\lambda_\mu(T, \omega)$. Furthermore, we observe that theory deviates consistently from experiment to lower values for energies greater than ~ 350 meV. This can also be traced to our use of the infinite band width approximation. A

more complete discussion of the effect of finite bands in the inverted electron-boson spectrum can be found in Ref.¹⁰.

Similar results are found for the B_{1g} data reconstruction. $\Gamma_{B_{1g}}(\omega, T)$ is reproduced equally well except for some deviations at low energies seen in the $T = 302$ K data because of a linear frequency dependence in the experimental $\Gamma_{B_{1g}}(\omega, T)$ data extending from ~ 100 meV down to $\omega = 0$ which cannot be reproduced by theory. Such a low energy linear dependence at room temperature has not been observed in the B_{2g} data [light open (black) dots in Fig. 2(a)]. The zero frequency offset of $\Gamma_{B_{1g}}(\omega \rightarrow 0, T)$ was compensated by an impurity scattering rate $\tau_{B_{1g},imp}^{-1} = 81.6$ meV about twice as much as was necessary for B_{2g} . The data reconstruction of the B_{1g} Raman cross section also reveals deviations from experiment at low and high frequencies which, again, can be understood to be the result of our infinite band approximation on which Eq. (2) is based.

We turn now to a comparison of antinodal with nodal Raman results of Figs. 1(a) and 1(b). The shapes of the distributions obtained are quite distinct. For B_{1g} there is a large peak at ~ 29 meV in the $T = 98$ K spectrum followed by a dip and then a second peak around 300 meV. As the temperature is increased there is a clear evolution of the spectrum with the low energy peak decaying in amplitude, broadening and moving towards higher energies. The same trend, although less pronounced, is observed for the second peak. The valley between the peaks becomes progressively filled in but it still very much remains, even for $T = 302$ K although the effects are much less pronounced. This is also seen when the B_{2g} (nodal) Raman spectrum is considered instead of B_{1g} (antinodal). The shape of $I_\mu^2\chi(\omega)$ for B_{1g} as well as its change with increasing temperature agrees well with previous trends for the optical case. In Fig. 1(c) we show results at $T = 100$ K, 200 K and 295 K in a sample of Bi2212 based on data by Tu *et al.*³⁶. The prominent peak is at a position (~ 44 meV) slightly different from our Raman spectrum, but the overall shape at 100 K is in good qualitative agreement with the Raman result [Fig. 1(a)] including the second peak, the valley between the two peaks, and the temperature evolution. A more extensive set of data on a similar sample but doped with some yttrium is found in Ref.¹². The data presented in their Fig. 2, top frame, is also in good qualitative agreement with our Raman results. The important observation is that both antinodal Raman and optical data show a prominent peak in the electron-boson spectral density around 30 to 40 meV which does not appear in ARPES and appears much less prominently in nodal Raman data. More specifically, the fractional area under this peak is only $\sim 3\%$ in B_{2g} as compared with $\sim 23\%$ in B_{1g} . As noted above, these two structures evolve with temperature in the same way which indicates their common origin. Part of this temperature evolution could be due to the reduced resolution intrinsic to our unbiased inversion method as the temperature is increased. (See Ref.¹⁷.) This is consistent with

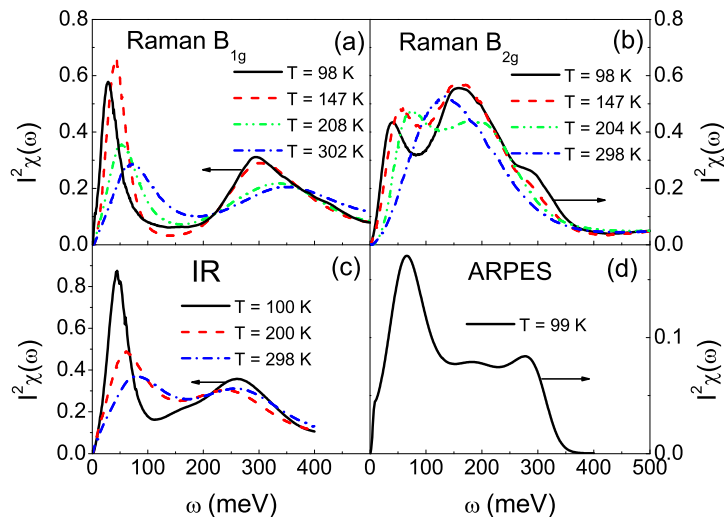


FIG. 1: (Colour on-line) The electron-boson spectral density (dimensionless) as a function of energy ω in meV from B_{1g} (a) and B_{2g} (b) Raman data. We show in (c) results¹⁷ obtained from optical data³⁶ and in (d) a result¹⁰ obtained from nodal direction ARPES⁶.

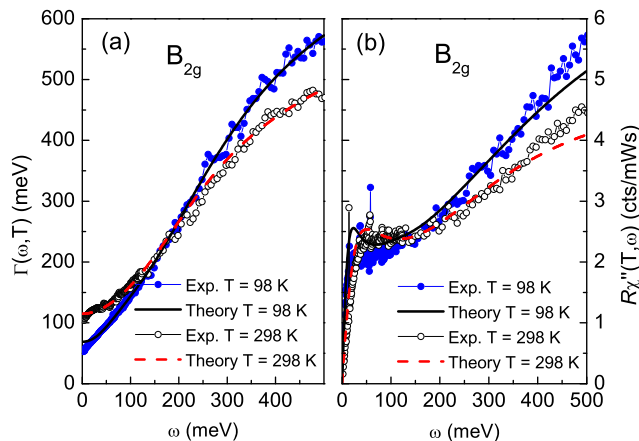


FIG. 2: (Colour on-line) (a) Fit to the B_{2g} Raman data for the scattering rate $\Gamma(\omega, T)$ from our maximum entropy reconstruction. (b) The corresponding fits to the measured B_{2g} cross section.

the results obtained with the biased inversion method discussed later in Fig. 3 which shows less temperature dependence.

For nodal ARPES there is no peak at ~ 30 meV but one appears instead at much higher energy ~ 65 meV. This higher energy has often been identified with coupling to oxygen phonons^{4-6,15,16} and we will return to this issue later. Such a peak is not seen in our Raman spectra which indicates that such effects are mainly confined to the nodal direction and do not appear in averaged quantities such as B_{1g} and even B_{2g} Raman even though for this latter polarization the Raman vertex peaks in the nodal direction. The fact that the peak at ~ 30 meV is stronger in B_{1g} (antinodal) than in B_{2g} (nodal) and is not

seen in nodal ARPES is consistent with a boson which is associated with scattering through momentum transfer \mathbf{q} of (π, π) . Such a vector corresponds to transitions between those parts on the Fermi surface which lie also on the antiferromagnetic Brillouin zone and is, therefore, closer to the antinodal direction. Consequently, quantities that emphasize the area around $(\pi, 0)$ such as B_{1g} Raman and, to some extent, optics should show a strong peak. In contrast, the peak at ~ 30 meV is expected to be weaker in B_{2g} symmetry weighing out the nodal part. This is what we observe and have shown in the data of Figs. 1(a) and (b).

Instead of using a maximum entropy technique to invert Eq. (2) van Heumen *et al.*¹⁴ used a histogram

to characterize the electron-boson spectral density, $I_{opt}^2\chi(\omega)$, derived from optics. The histogram is then used to directly reconstruct the experimental data by inversion of Eq. (5) modified for the optical conductivity. They find less temperature dependence than we have here, for the position and width of the peak around 30 meV in B_{1g} . So far we used an *unbiased* maximum entropy inversion of Eq. (2) in which the default model¹⁷ is set to a constant at all temperatures. Another method is the so-called *biased* maximum entropy inversion in which the default model is set to the previous next lower temperature solution. We can expect the solutions of these two methods to be different because the inversion of Eq. (2) is an ill-posed problem which usually has more than one solution. It was pointed out by Yang *et al.*¹⁹ that in the case of $\text{HgBa}_2\text{CuO}_{4+\delta}$ the biased inversion of optical data resulted in electron-boson spectra very similar to those reported by van Heumen *et al.*¹⁴ for the same material.

Results of such a biased inversion of the Raman B_{1g} and B_{2g} data are shown in Figs. 3(a) and 3(b), respectively. We see that the peak at ~ 30 meV for the B_{1g} spectra shifts less with temperature than is shown in Fig. 1(a) although it still loses amplitude with increasing temperature T . This points to the possibility that at least part of this peak comes from a phonon, and its contribution could be determined from the amplitude of this peak at room temperature. The situation is quite different for the B_{2g} polarization. Comparison of the spectra shown in Fig. 3(b) with the ones presented in Fig. 1(b) reveals that there is very little difference between the two sets of spectra. In particular, the position of the low energy peak (~ 40 meV at 98 K) shows almost the same temperature dependence and is almost smeared out at room temperature. Furthermore, the inversion method has little or no influence on the shape and size of the high energy part ($\omega > 100$ meV) of the B_{1g} and B_{2g} spectra. Figures 3(c) and 3(d) show results for the often used mass enhancement parameter $\lambda_\mu = 2 \int_0^\infty d\omega I_\mu^2\chi(\omega)/\omega$ as a function of temperature for B_{1g} and B_{2g} polarization, respectively. There is very little difference between the two methods of inversion.

Returning to Fig. 1(b), the nodal direction Raman spectrum (B_{2g}) has a very different characteristic shape as compared to B_{1g} , Fig. 1(a). While it can be characterized as also having two peaks, the valley between them is not pronounced and its spectral weight is much more uniformly distributed below 300 meV with a relatively sharp drop off beyond this energy. This shape is much closer to what has been found in inversions of the nodal direction ARPES data reproduced in Fig. 1(d). This is expected since the B_{2g} Raman vertex peaks at the nodal direction. Note that ARPES is strictly directional and samples only the nodal direction while B_{2g} Raman probes an extended part of the BZ weighted by $\sin^2(2\theta)$. Nevertheless, the agreement as to shape between B_{2g} Raman and nodal direction ARPES gives one confidence that both methods are measuring the same boson spectrum. Note that there is nothing which limits the application of this method to

the high- T_c cuprates and our inversion technique has a more general applicability to other metals.

While our inversions provide us with a good handle on the size and qualitative shape of the spectral density, the question as to the origin of the boson involved is more difficult to answer in a definite way. Certainly if phonons are involved we would expect $I_\mu^2\chi(\omega)$ to mirror the phonon frequency distribution while for spin fluctuations we should see an image of the local spin susceptibility. The fact that $I_\mu^2\chi(\omega)$ shows very significant spectral weight up to 400 meV means that excitations other than phonons having energies below 100 meV are involved. For spin fluctuations the energy scale is set by the exchange coupling, J , which enters, e.g., the $t - J$ model as a parameter, and this is consistent with the large energy scale seen here. It is also consistent with recent numerical studies of the $t - J$ model by Maier *et al.*³⁷ in which an effective electron-boson spectral density associated with short range spin fluctuations is extracted and identified as the pairing glue. It displays many of the features seen in our empirical spectra. The cellular dynamical mean-field calculations of Kyung *et al.*³⁸ based on the Hubbard model also give qualitatively similar results for the spectral density and offer further microscopic support for an interpretation of our derived spectra as due largely to spin fluctuations.

On the other hand one does expect, and experimental data provide support for some contribution from the electron-phonon interaction^{3,5-7}. While the change in critical temperature T_c on substitution of $^{16}\text{O} \rightarrow ^{18}\text{O}$ is small for optimally doped samples, it is nonzero and it can be large for the underdoped case. However, the latter fact can also be understood as due to an energy dependence in the electronic density of states³⁹ or to a pseudogap formation⁴⁰ while at the same time the underlying contribution of phonons to the pairing interaction remains small. Recent ARPES experiments along the nodal direction¹⁶ found a shift in the ‘boson kink’ in the renormalized dispersion curves of Bi2212 upon oxygen isotope substitution. This was assigned by Schachinger *et al.*¹⁵ as a 10% phonon contribution to the electron-boson spectral density found in inversions¹⁰ of ARPES data as reproduced in Fig. 1(d). They assign the peak around 65 meV to electron-phonon effects and the rest due to spin fluctuations. Accounting for finite band effects this translates into a contribution to the quasiparticle mass enhancement due to phonons of $\lambda \simeq 0.2$ at a temperature of $T = 17$ K. A similar estimate was found by Devereaux *et al.*⁴¹ due to the buckling and breathing phonon modes. Recent calculations based on local-density approximation also predict mass enhancements due to phonons⁴²⁻⁴⁵ but are up to an order of magnitude smaller than our result.

The aim of this work was to extract from the electronic Raman cross section in B_{1g} and B_{2g} (μ) symmetry, the corresponding electron-boson spectral density $I_\mu^2\chi(\omega)$. Comparison with equivalent, previously extracted forms from optical and nodal ARPES data shows remarkable consistency between the results obtained with such dif-

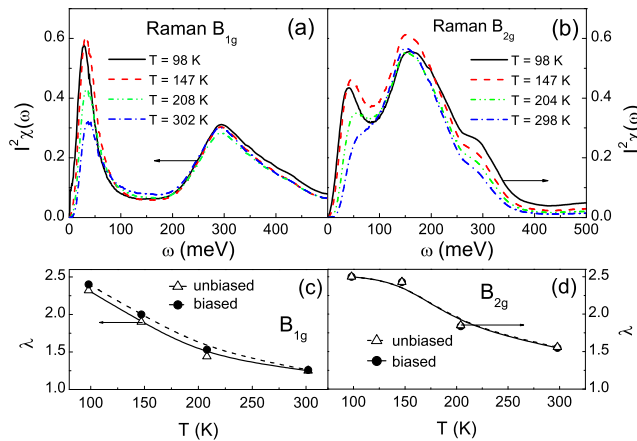


FIG. 3: (Colour on-line) (a) The electron-boson spectral density $I^2\chi(\omega)$ (dimensionless) as a function of energy ω in meV from B_{1g} Raman scattering rates using a biased maximum entropy inversion as described in the text. (b) The same as (a) but now for B_{2g} symmetry. Frames (c) and (d) compare the temperature dependences of the mass enhancement parameters λ obtained from biased and unbiased inversion of the B_{1g} and B_{2g} Raman scattering rates, respectively.

ferent probes. Comparison of these results provides information on the angular variation of the electron-boson self energy and corresponding spectral density around the Fermi surface. This arises because optics involves an average over the entire Fermi surface while Raman weights predominantly the antinodal and the nodal directions for B_{1g} and B_{2g} symmetry, respectively. Only ARPES is perfectly directional. While we now have a good handle on the size and qualitative shape of the spectral density, the question of what bosons might be involved is more difficult. Certainly, the general shape of the $I^2\chi(\omega)$ should reflect the phonon frequency distribution if the electron-phonon interaction is dominant while it should mirror the shape of the local spin susceptibility if it is, instead, the spin fluctuations that are dominant. The fact that all spectral functions obtained have very significant spectral weight beyond 100 meV makes it clear that ex-

citations other than phonons are primarily involved. An energy scale set by J is more consistent with our results.

Acknowledgments

This Research was supported in part by the Natural Sciences and Engineering Research Council of Canada (NSERC) and by the Canadian Institute for Advanced Research (CIFAR). The group in Garching gratefully acknowledges support by the German Research Foundation (DFG) via grant No. Ha 2071/3 in the Research Unit FOR538. E. S. acknowledges support by the Austrian Research Fund (FWF), Vienna, contract No. P18551-N16.

* Electronic address: schachinger@itp.tu-graz.ac.at

¹ J. F. Zasadzinski *et al.*, Phys. Rev. Lett. **96**, 017004 (2006).
² J. Lee *et al.*, Nature (London) **442**, 546 (2006).
³ A. N. Pasupathy *et al.*, Science **320**, 196 (2008).
⁴ A. Lanzara *et al.*, Nature (London) **412**, 510 (2001).
⁵ T. Cuk *et al.*, Phys. Rev. Lett. **93**, 117003 (2004).
⁶ X. J. Zhou *et al.*, Phys. Rev. Lett. **95**, 117001 (2005).
⁷ W. Meevasana *et al.*, Phys. Rev. Lett. **96**, 157003 (2006).
⁸ T. Valla *et al.*, Phys. Rev. Lett. **98**, 167003 (2007).
⁹ A. A. Kordyuk *et al.*, Phys. Rev. Lett. **97**, 017002 (2006).
¹⁰ E. Schachinger and J. P. Carbotte, Phys. Rev. B **77**, 094524 (2008).
¹¹ E. Schachinger and J. P. Carbotte, Phys. Rev. B **62**, 9054 (2000).
¹² J. Hwang, T. Timusk, E. Schachinger, and J. P. Carbotte, Phys. Rev. B **75**, 144508 (2007).

¹³ E. Schachinger, J. J. Tu, and J. P. Carbotte, Phys. Rev. B **67**, 214508 (2003).
¹⁴ E. van Heumen *et al.*, Phys. Rev. B **79**, 184512 (2009).
¹⁵ E. Schachinger, J. P. Carbotte, and T. Timusk, EPL **86**, 67003 (2009).
¹⁶ H. Iwasawa *et al.*, Phys. Rev. Lett. **101**, 157005 (2008).
¹⁷ E. Schachinger, D. Neuber, and J. P. Carbotte, Phys. Rev. B **73**, 184507 (2006).
¹⁸ J. F. Zasadzinski *et al.*, Phys. Rev. Lett. **87**, 067005 (2001).
¹⁹ J. Yang *et al.*, Phys. Rev. Lett. **102**, 027003 (2009).
²⁰ J. P. Carbotte, E. Schachinger, and J. Hwang, Phys. Rev. B **71**, 054506 (2005).
²¹ T. P. Devereaux *et al.*, Phys. Rev. Lett. **72**, 396 (1994).
²² D. Branch and J. P. Carbotte, J. Supercond: Novel Magnetism **13**, 535 (2000).
²³ D. Branch and J. P. Carbotte, Phys. Rev. B **52**, 603 (1995).

- ²⁴ C. Jiang and J. P. Carbotte, Phys. Rev. B **53**, 11868 (1996).
- ²⁵ M. Opel *et al.*, Phys. Rev. B **61**, 9752 (2000).
- ²⁶ T. Devereaux and R. Hackl, Rev. Mod. Phys. **79**, 175 (2007).
- ²⁷ B. Muschler *et al.*, Eur. Phys. J. Special Topics to be published (2010).
- ²⁸ E. J. Nicol, J. P. Carbotte, and T. Timusk, Phys. Rev. B **43**, 473 (1991).
- ²⁹ F. Marsiglio, J. P. Carbotte, A. Puchkov, and T. Timusk, Phys. Rev. B **53**, 9433 (1996).
- ³⁰ J. P. Carbotte, C. Jiang, D. N. Basov, and T. Timusk, Phys. Rev. B **51**, 11798 (1995).
- ³¹ E. Schachinger, J. P. Carbotte, and F. Marsiglio, Phys. Rev. B **56**, 2738 (1997).
- ³² C. Jiang *et al.*, Phys. Rev. B **54**, 1264 (1996).
- ³³ F. Marsiglio, T. Startseva, and J. P. Carbotte, Physics Lett. A **245**, 172 (1998).
- ³⁴ S. V. Shulga, O. V. Dolgov, and E. G. Maksimov, Physica C **178**, 266 (1991).
- ³⁵ S. G. Sharapov and J. P. Carbotte, Phys. Rev. B **72**, 134506 (2005).
- ³⁶ J. J. Tu *et al.*, Phys. Rev. B **66**, 144514 (2002).
- ³⁷ T. A. Maier, D. Poilblanc, and D. J. Scalapino, Phys. Rev. Lett. **100**, 237001 (2008).
- ³⁸ B. Kyung, D. Sénéchal, and A.-M. S. Tremblay, Phys. Rev. B **80**, 205109 (2009).
- ³⁹ E. Schachinger, M. G. Greeson, and J. P. Carbotte, Phys. Rev. B **42**, 406 (1990).
- ⁴⁰ T. Dahm, Phys. Rev. B **61**, 6381 (2000).
- ⁴¹ T. P. Devereaux, T. Cuk, Z.-X. Shen, and N. Nagaosa, Phys. Rev. Lett. **93**, 117004 (2004).
- ⁴² R. Heid, K.-P. Bohnen, R. Zeyher, and D. Manske, Phys. Rev. Lett. **100**, 137001 (2008).
- ⁴³ S. Y. Savrasov and O. K. Andersen, Phys. Rev. Lett. **77**, 4430 (1996).
- ⁴⁴ K. P. Bohnen, R. Heid, and M. Krauss, EPL **64**, 104 (2003).
- ⁴⁵ F. Giustino, M. L. Cohen, and S. G. Louie, Nature (London) **452**, 975 (2008).